nature nanotechnology

SUPPLEMENTARY INFORMATION

https://doi.org/10.1038/s41565-018-0097-z

In the format provided by the authors and unedited.

Highly efficient solar vapour generation via hierarchically nanostructured gels

Fei Zhao[1,4], Xingyi Zhou[1,4], Ye Shi[1], Xin Qian[2], Megan Alexander[1], Xinpeng Zhao[2], Samantha Mendez[1], Ronggui Yang[2]*, Liangti Qu[3]* and Guihua Yu[1]*

[1]Materials Science and Engineering Program and Department of Mechanical Engineering, The University of Texas at Austin, Austin, TX, USA. [2]Department of Mechanical Engineering, University of Colorado, Boulder, CO, USA. [3]Key Laboratory of Photoelectronic/Eletrophotonic Conversion Materials, School of Chemistry and Chemical Engineering, Beijing Institute of Technology, Beijing, China. [4]These authors contributed equally: F. Zhao, X. Zhou. *e-mail: ronggui.yang@colorado.edu; lqu@bit.edu.cn; ghyu@austin.utexas.edu

Highly efficient solar vapor generation via hierarchically nanostructured gels

Fei Zhao,[1†] *Xingyi Zhou,*[1†] *Ye Shi,*[1] *Xin Qian,*[2] *Megan Alexander,*[1] *Xinpeng Zhao,*[2]

Samantha Mendez,[1] *Ronggui Yang,*[2*] *Liangti Qu,*[3*] *and Guihua Yu*[1*]

* Correspondence to: ghyu@austin.utexas.edu; lqu@bit.edu.cn;

ronggui.yang@colorado.edu.

† These authors contributed equally to this work

Supplementary Information

Contents

S1. Supplementary Methods

S1.1 Chemicals and materials

Chemicals including polyvinyl alcohol (PVA) with average molecular weight of 15 000, HCl, pyrrole, glutaraldehyde, ammonium persulfate (APS) were purchased from Sigma-Aldrich.

S1.2 Fabrication procedure

S1.2.1 Preparation of polypyrrole (PPy)

For the preparation of PPy, 0.228g of APS was dissolved in 10 mL deionized (DI) water, and labelled as solution A. 0.069 mL pyrrole was uniformly mixed with 10 mL DI water by sonication for 10 min and labelled as solution B. Adding the solution A and B dropwise in turn to 50 mL 1.2 M HCl aqueous solution with stir. The polymerization was carried out for 5 min, the purification of as-prepared PPy can be achieved by washing and filtration by DI water for 3 times. The purified PPy was then well dispersed in DI water by sonication to form PPy solution.

S1.2.2 Preparation of hierarchically nanostructured gel (HNG)

In a typical synthesis, PVA (1 g), glutaraldehyde (125 μL, 50%wt in DI water) and DI water (10 mL) were mixed together by sonication (solution C). Then HCl (50 μL, 1.2 M) and PPy (100 μL, 10%wt) solution were added to 1 mL of solution C, the gelation was carried out for 2 h. The obtained PVA gel was immersed into DI water overnight to obtain pure HNGs. The purified HNG was frozen by liquid nitrogen and then thawed in DI water at a temperature of 30 ºC. The freezing-thawing process was repeated for 10 times. Finally, the obtained HNG sample was freeze-dried.

S1.2.3 Preparation of PVA gel (control sample 1)

In a typical synthesis, PVA (1 g), glutaraldehyde (125 μL, 50%wt in DI water) and DI water (10 mL) were mixed together by sonication (solution D). Then HCl (50 μL, 1.2 M) solution was added into 1 mL of solution D, the gelation was carried out for 2 h.

The obtained PVA gel was immersed into DI water overnight to obtain pure PVA gel. The purified PVA gel was frozen by liquid nitrogen and then thawed in DI water with a temperature of 30 ºC. The freezing-thawing process was repeated for 10 times. Finally, the obtained PVA gel sample was freeze-dried.

S1.2.4 Preparation of PVA/PPy gel (control sample 2)

In a typical synthesis, PVA (1 g), glutaraldehyde solution (125 μL, 50%$_{wt}$ in DI water) and DI water (10 mL) were mixed together by sonication (solution D). Then HCl (50 μL, 1.2 M) solution was added into 1 mL of solution D, the gelation was carried out for 2 h. The obtained PVA gel was immersed into DI water overnight to obtain pure PVA gel. The purified PVA gel was immersed into pyrrole solution (1 mL, 20 %$_{wt}$ in DI water) for 24 h to prepare PVA gel with pyrrole infiltrative (ca. 10%$_{wt}$). The obtained gel was immersed into APS solution (0.1M) for 1 h to prepare PVA/PPy gel, where the color change from light yellow to black. The as-prepared PVA/PPy gel was purified by DI water. The purified sample was frozen in liquid nitrogen and then thawed in DI water with a temperature of 30 ºC. The freezing-thawing process was repeated for 10 times. Finally, the obtained PVA gel sample was freeze-dried.

S1.3 Water transport measurements

The completely dried samples of HNG were immersed in DI water at a temperature of 40 ºC. The weight of these samples was carefully tracked during the swollen process until they were fully hydrated (no weight change in 30 min). The record data from half-hydrated to fully-hydrated was used to evaluate the water transport in HNGs.

S2. Supplementary Figures

S2.1 Introducing internal gaps in the polymeric skeleton of gels.

The gelation process of monomers was achieved by simultaneous polymerization and cross-linking. As shown in Supplementary Fig. 1a, the monomer is bonded with each other to form oligomers. Then the further growth of oligomer chains was realized by the monomer-oligomer and oligomer-oligomer reactions. Meanwhile, upon the presence of cross-linker, the as-formed oligomers are cross-linked, constructing the network. Owing to the well-dissolved monomers (and oligomers), the porosity of obtained polymeric network are uniform in different parts of the gel. On the contrary, in the current work, the basic building block was the clusters dispersed in water, which were constructed by hydrophobic PPy and amphiphilic (surfactant) PVA. The gelation depends on the cross-linking of PVA chains. Therefore, in the cluster, the cross-linked PVA provided a polymeric network similar with that of in normal gels, producing micro-gel (Supplementary Fig. 1b). On the interfaces, the cross-linking enabled a connection of two micro-gels, leaving spacing in the PVA matrix, hence forming the internal gaps in the resultant gels.

As presented in main text, the scanning electron microscope (SEM), the rheology test and the Fourier transform infrared (FTIR) spectroscopy can be used to characterize the porous structure, the structure of polymeric network and the chemical state of every component, respectively. SEM imaging not only directly shows the presence of internal gap and micro-channels, but also reflects their spatial distribution. Since the rheological behavior is determined by the skeleton of gels, the rheology test is an effective way to reveal the structure of polymeric network. Generally, the interaction between polymers and nanoscale light absorbers can reinforce the network, inducing a higher storage modulus (G') and the loss modulus (G"). The FTIR is a standard method to trace the typical functional groups in organic materials. Such technique can be used to confirm whether the typical functional group in polymers, absorbers and other components are

retained after the gelation, confirming if the chemical state of the obtained gel is consistent with the design.

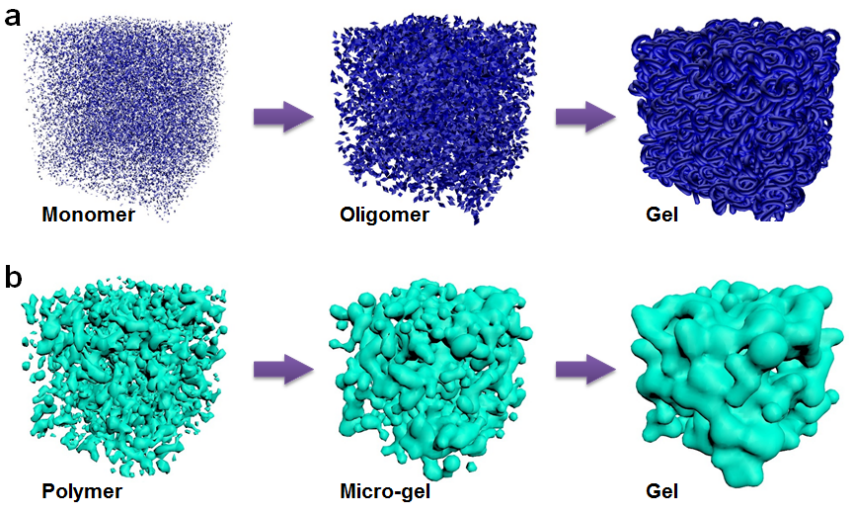

Supplementary Figure 1. Different strategies of polymeric gel preparation. Preparing gels from (a) dissoluble monomers and (b) dispersing polymer clusters.

S2.2 Flexibility and elasticity of HNG.

The HNG shows good mechanical stability during the bending (Supplementary Fig. 2a) and compression (Supplementary Fig. 2b) tests with bending radii of 1 cm and weight loading of 200 grams, respectively. Moreover, the compression test was performed to quantitatively determine the mechanical properties of HNG. As shown in Supplementary Fig. 2c, a representative stress-strain curve for the HNG was presented with a fracture strain of 16 % occurred with the stress of 0.38 MPa, meeting the mechanical requirement of operation in practical solar vapor generation.

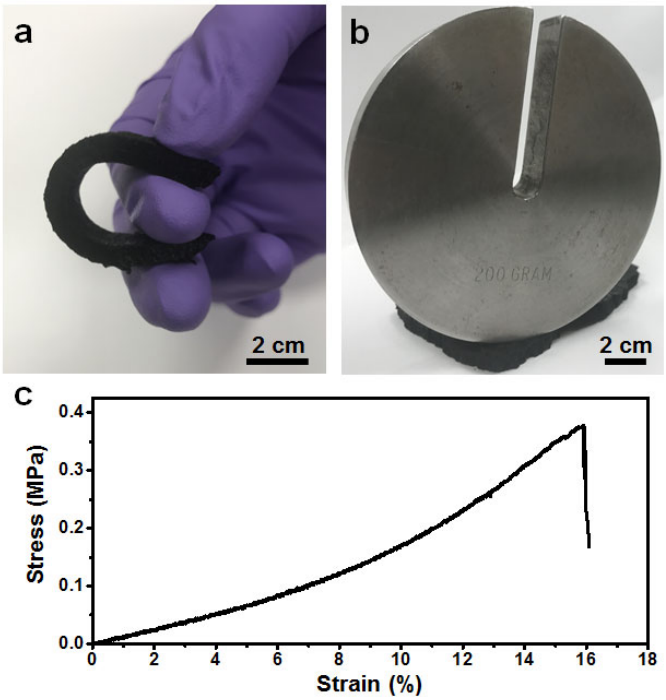

Supplementary Figure 2. Photographs of (a) bending and (b) compression tests of HNG samples. (c) Compressive stress–strain curve of the HNG.

S2.3 The swelling ratio of the wall structure in HNG.

To estimate the swollen behavior of wall structure in HNG, a PVA/PPy gel (without hierarchical nanostructure) was prepared as a control sample, where the py monomer was introduced and polymerized after the formation of PVA skeleton (See *Supplementary Methods S1.2.4* for detail). In view of the excellent water solubility of PVA, the PVA/PPy gel was uniformly constructed by the polymeric network of PVA after gelation (i.e. crosslinking process). Therefore, the swollen behavior of wall structure in HNG could be revealed by the swelling ratio of PVA gel. The repeatable shrinking-swelling process enabled a thickness change between ca. 0.6 mm to ca. 4.1 mm (Supplementary Fig. 3a). The calculated swelling ratio along the dimension of thickness was ca. 700 %, suggesting a similar estimated swollen ratio of the wall structure in HNG (Supplementary Fig. 3b).

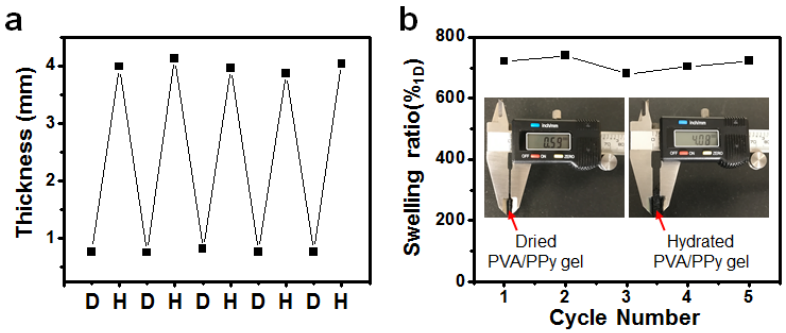

Supplementary Figure 3. (a) The thickness of dried (D) and hydrated (H) state PVA/PPy gel. (b) Calculated swelling ratio upon the dimension of thickness; Insets, the thickness test of dried and hydrated PVA/PPy gel.

S2.4 Investigation of PPy penetration in PVA skeleton

In the view that the polymeric skeleton dominates mechanical properties of gels, G′ and G″ values can represent the structural variation of polymer network (e.g. penetrated by other polymers)[S1]. Therefore, PVA/PPy gel, the control sample, was used to further illustrate the interpenetration of PVA and PPy in HNGs. The G′ and G″ values of PVA gel, HNG and PVA/PPy gel with water as a solvent are shown in Supplementary Fig. 4. Their gel states are revealed by the wide linear viscoelastic region in the dynamic frequency sweep experiments and further confirmed by the fact that the value of storage modulus is higher than that of the loss modulus in each case. The PVA/PPy sample shows identical G′ and G″ value with that of pure PVA gel, which is attributed to the similar skeleton structure brought by the continuous flexible polymeric networks of PVA. The influence of relatively rigid PPy attached on the PVA backbones can be ignored. On the contrary, the G′ and G″ value of HNG are significantly lower than that of PVA gel, indicating a weakened skeleton. As discussed in Supplementary Fig. 1, the basic building blocks were the PVA/PPy clusters dispersing in water. It means that the PPy chains were interpenetrated with PVA chains, changing the cross-linking process of PVA, hence resulting different polymeric skeleton compared with PVA gel. Therefore, the PPy was inlaid to the polymeric network of PVA in HNGs.

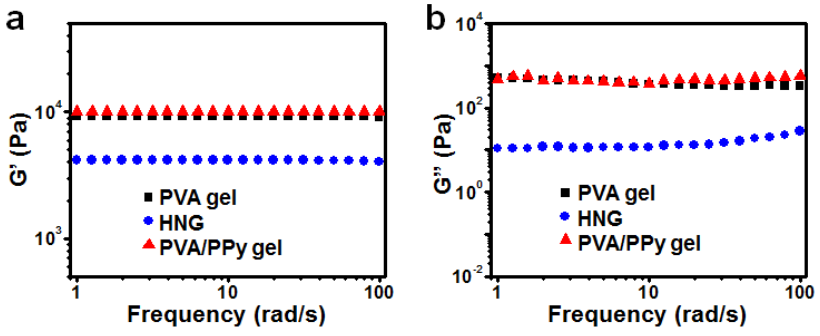

Supplementary Figure 4. (a) the storage modulus (G') and (b) loss modulus (G") of PVA gel, HNG and PVA/PPy gel tested in a frequency sweep mode.

S2.5 Chemical composition of HNG.

Supplementary Fig. 5 shows the TGA patterns of PVA gel, PPy and HNG after pre-drying under 100 ºC for 5 h. For a temperature from 100 to 230 °C, all the samples show an initial weight loss. This weight loss is attributed to the evaporation of physically adsorbed water molecules and the removal of unreacted monomers from their surface[S2]. The second weight loss starts from 320 °C to 460 °C for the PVA sample, while 230 °C to 700 °C for PPy sample, corresponding to the disintegration of PPy and PVA polymer chains. Therefore, the weight loss of HNG sample could be attributed to rapid decomposition of PVA (from 320 °C to 460 °C) and gradually decomposed PPy (from 230 °C to 700 °C). It is important to note that decomposition rate of HNG altered at 410 °C, which is ca. 60 °C higher than the temperature that decomposition rate of PPy altered, suggesting a stabilized PPy in HNG owing to its penetration in PVA network.

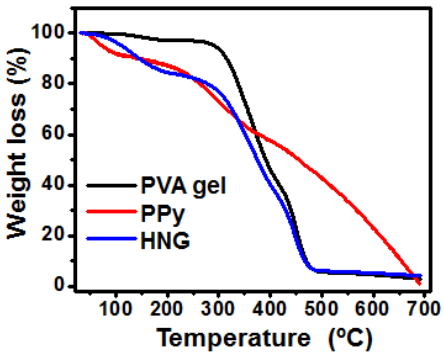

Supplementary Figure 5. The TGA of as-prepared PVA aerogel, PPy and HNG.

S2.6 Optimization of PPy/PVA ratio.

The optimized weight ratio of polypyrrole/polyvinyl alcohol (PPy/PVA) is 0.1:1 in HNGs. An optimized PPy/PVA ratio can enable the accelerated solar vapor generation and reduce the cost of PPy. As shown below, solar vapor generation of the control samples with PPy/PVA weight ratio of 0.003:1, 0.01:1, 0.1:1, 0.5:1 and 1:1, designating as GP-(Gels with PPy/PVA ratio of) 0.003, GP-0.01, GP-0.1, GP-0.5 and GP-1, respectively, were tested under one sun. Since the water/PVA ratio of theses control samples was 10:1, GP-0.1 was the HNG3 mentioned in main text. The corresponding solar evaporation rates of GP-0.003 to GP-1 were ca. 0.6, ca. 1, ca. 3, ca. 2.9 and ca. 3 kg/m^2/h. Thus, an optimized PPy/PVA ratio in HNG was proposed to be 0.1:1. These results can be attributed to the nanostructure variation caused by PPy/PVA ratio change.

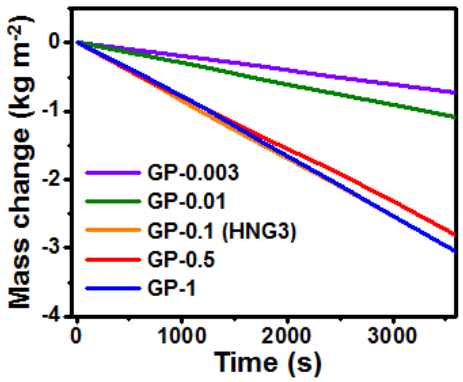

Supplementary Figure 6. Mass change over time with GP-0.003, GP-0.01, GP-0.1, GP-0.5 and GP-1.

As shown in Supplementary Fig. 7, the GP-0.003 (Supplementary Fig. 7a), GP-0.01 (Supplementary Fig. 7b), GP-0.5 (Supplementary Fig. 7c) and GP-1 (Supplementary Fig. 7d) presented similar micro-channels. The GP-0.5 and GP-1 exhibit internal gaps (red dash), while the GP-0.003 and GP-0.01 only provide the micro-channels. Thus, the PPy/PVA ratio should be larger than 0.1:1 to achieve the hierarchical nanostructure.

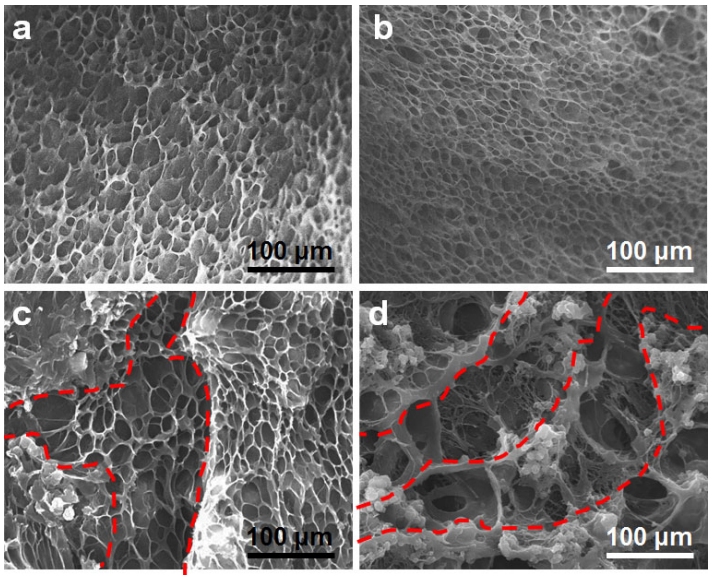

Supplementary Figure 7. SEM images of (a) GP-0.003, (b) GP-0.01, (c) GP-0.5 and (d) GP-1. The internal gaps were delineated by red dashes.

The mechanical property further evidenced such difference among gels with different PPy/PVA ratio. The stress at fracture for the hybrid gels was about 0.4 MPa, while the fracture strain increases gradually from 33 % to 81% as the PPy/PVA ratio increases from 0.003:1 to 1:1. According to the gel elasticity theory, the similar stress at fracture indicates mechanical strength of polymeric skeleton, and the increased fracture strain evidenced large free-space (i.e. internal gaps) in the gel, which is in agreement with the microscopic observation.

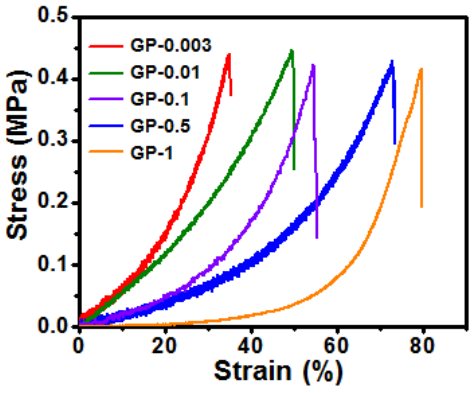

Supplementary Figure 8. Mechanical properties of gels with different PPy/PVA ratio.

S2.7 Water absorbing experiment.

Water transport in polymeric gels can be represented by their swollen behavior. Water transport in internal gaps and micron channels was enabled by capillary pumping, while water diffusion to molecular meshes depended on the osmosis effect. Thus, the swelling of the polymeric network (i.e. water transport to the molecular meshes) dominated the water absorbing rate. In this context, the HNGs with water/PVA weight ratio of 1:0.2, 1:0.15, 1:0.1 and 1:0.075 were prepared and noted as HNG1, HNG2, HNG3 and HNG4. The swollen behavior of these HNGs was investigated to evaluate the microstructure dependent water transport.

The water content (Q) was represented by the weights of water in the fully swollen sample per gram of corresponding dried xerogel sample, respectively. Note that the Q value here was measured from HNG samples which were wiped by bibulous paper. Owing to the strong capillary of bibulous paper, most of the water in internal gaps and micron channels was removed. As shown in Fig. 3a, the Q_s value of HNG4 was up to 7.6 g per gram of the corresponding dried sample (i.e. g g^{-1}), which is ~ 1.4, 2.5 and 5.5 times higher than that of HNG3, HNG2, and HNG1, respectively, indicating that a large range of Qs values can be obtained by adjusting the PVA concentration. On the other hand, the dynamic analysis of the swelling process was carried out to evaluate the water transport in HNGs. The water content of HNGs was carefully reduced to $0.5Q_s$ by a pretreatment, realizing a half-saturated state. The swollen time from half-saturated state to saturated state revealed the water transport in the HNGs (Fig. 3b). Since all the Q values of HNG1 to HNG4 present linear dependence on time during the swelling, a water transport rate (V) was defined as water absorption per minute. Upon one gram of xerogel, the HNG1, HNG2, HNG3 and HNG4 showed V value of 0.016, 0.04, 0.083 and 0.127 g min^{-1}, indicating that the nanostructured channels facilitate water transport (Supplementary Fig. 10 and 11). As shown in Supplementary Fig. 9a, the dynamic analysis of the swelling process was carried out to evaluate the water transport in HNGs. The water content of HNGs was carefully reduced to $0.5Q_s$ by a pretreatment, realizing

a half-saturated state. The swollen time from the half-saturated state (50% of the Q_s) to saturated state (100% Q_s) was showed in Supplementary Fig. 9b.

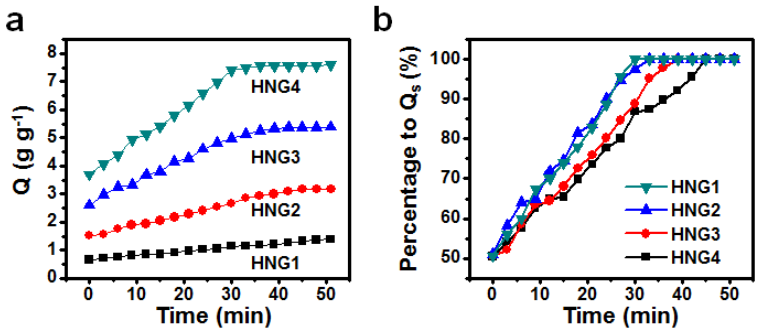

Supplementary Figure 9. (a) Water content (Q) variation over time and (b) percentage to the corresponding saturated water content (Q_s) of each sample.

S2.8 Microscopic structure dominated by Water/PVA ratio.

A tailored 3D hierarchical network of channels can facilitate water transport in HNGs. Thus, the SEM images were used to observe the porous structure of HNGs. As shown below, the porous size of HNG1, HNG2, HNG3 and HNG4 changed from several microns to 10-20 microns.

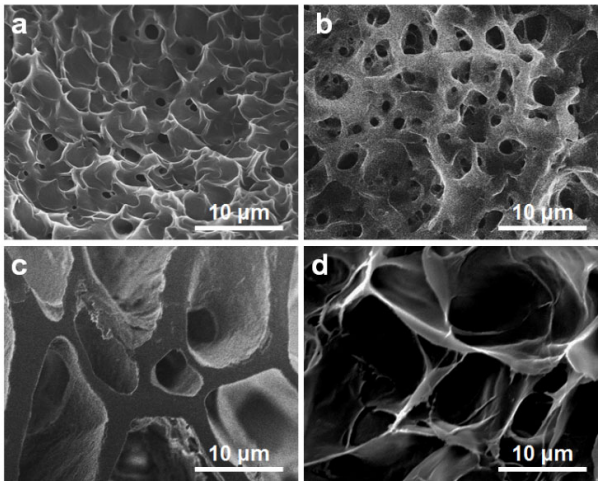

Supplementary Figure 10. SEM images of (a) HNG1, (b) HNG2, (c) HNG3 and (d) HNG4, showing the wall structure with different thickness.

Additionally, the thickness of their wall-structures also varied, which resulted in different mechanical properties. The representative stress-strain curves for the HNG1, HNG2, HNG3 and HNG4 were presented. The stress at fracture for the HNGs decreased gradually from 0.49 to 0.26 MPa with the corresponding fracture strain from 33 to 62 %, indicating enhanced crosslinking in HNGs with higher PVA/water ratio.

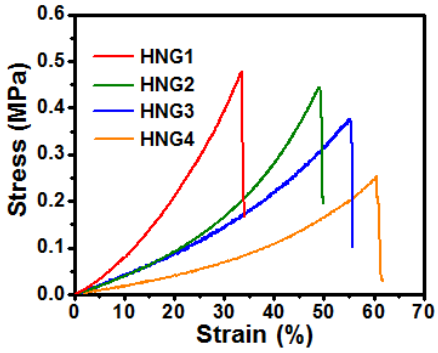

Supplementary Figure 11. Mechanical properties of HNGs.

S2.9 Evaluation of light absorption.

The reflectance and transparency of the HNG samples were studied by a UV–vis–NIR spectrophotometer. All the HNG sheets (from HNG1 to HNG4) presented relatively lower reflectance (<5%) in a wide wavelength range from 350 to 2500 nm (Supplementary Figure 12a). The reflectance of HNG is not sensitive to the chemical composition. Additionally, Since the transparency depended on the thickness of absorber, the transmittance of HNGs with different thickness was carefully measured. For comparison, we measured the transparency of HNG3 sheets with different thickness. The HNG3 sheet with a thickness of 387 μm appears to be the optimum one for the full spectral absorption of solar illumination (Supplementary Figure 12b). Thus, the thickness of the effective solar energy harvesting region in HNGs was around 400 μm. These results revealed a solar energy harvesting efficiency over 95 % using an HNG3 sheet.

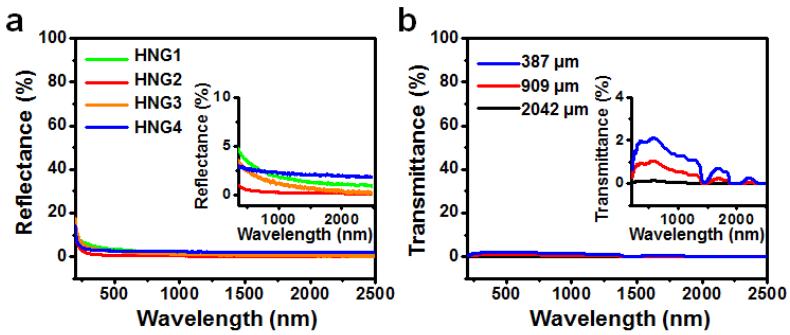

Supplementary Figure 12. (a) Reflectance and (b) transmittance spectra of the HNG samples in the wavelength range of 200–2500 nm. Insets: High resolution curves of (a) reflectance and (b) transmittance.

S2.10 Dependence of saturated water content and water transport on thickness.

Since the thickness of HNG samples in the solar vapor generation test is about 0.8 mm, the samples with thickness from 0.4 to 2 mm was used to evaluate the dependence of Q_s (Supplementary Figure 13a), V (Supplementary Figure 13b) on thickness. The results here indicated that the Q_s and V are independent on thickness.

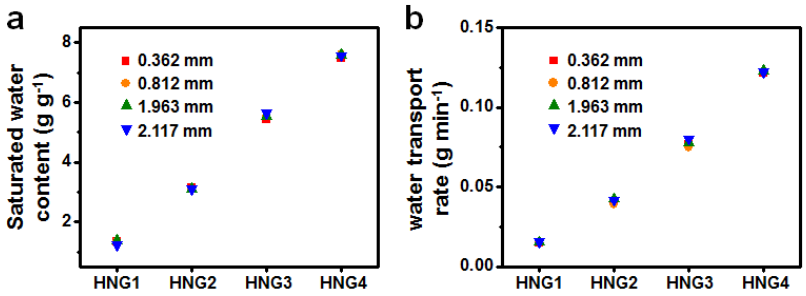

Supplementary Figure 13. (a) Saturated water content and (b) calculated water transport rate of HNG samples with different thickness.

S2.11 Solar heating behavior of dehydrated HNGs.

To further show the highly efficient solar thermal utilization in the HNGs, the containing water was completely removed. The dehydrated HNGs (from HNG1 to HNG4) could be identical heat to ca. 85 ºC within 2 min and the temperature was gradually raised to 90 ºC in another 4 min (Supplementary Figure 14). It means that the main part of converted energy was consumed by the water when those gels were fully hydrated, demonstrating the highly efficient energy utilization.

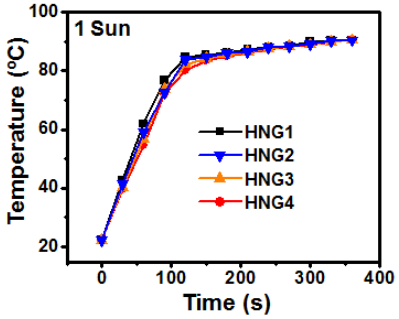

Supplementary Figure 14. The surface temperature of freezing-dried HNGs under solar illumination of 1 kW m^{-2} as a function of irradiation time.

S2.12 Vapor generation of HNGs under concentrated solar radiation.

In the control experiments under optically concentrated solar radiation, the HNG3 exhibited best solar vapor generation rate comparing with HNG1, HNG2 and HNG4. It is obvious that vapor generation was accelerated under all of the optical concentration conditions (Supplementary Figure 15). For example, the evaporation rate with the HNG3 under 4 kW m^{-2} reaches ca. 6.2 kg m^{-2} h^{-1}, which is 1.9 times that of 1 kW m^{-2} experiment. Theoretically, the concentrated solar irradiation could enable a higher input energy density, resulting in localized heating, hence facilitating the water evaporation and improving the energy utilization efficiency[S3-S6]. The increasing ratio of water evaporation rate should be approximately equivalent to the enhancement ratio of solar radiation. However, in the current work, when the solar radiation was enhanced, the water transport rate of HNG1, HNG2 and HNG3 were relatively low. As a result, these HNGs presented limited increasing of evaporation rate under concentrated solar radiation. In contrast, benefiting from higher water content and water transport rate the HNG4 provided an evaporation rate of ca. 4.4 kg m^{-2} h^{-1} under 4 sun, which was over 6 times than that of under 1 sun. This means that such water content is relatively appropriate for 4 sun radiation despite excessive for 1 sun. In another word, the water content dominates the water evaporation under weak solar radiation, while water transport rate becomes an important factor with stronger solar concentration. These results further demonstrated the importance of Q/V balance, in agreement with the applied solar radiation.

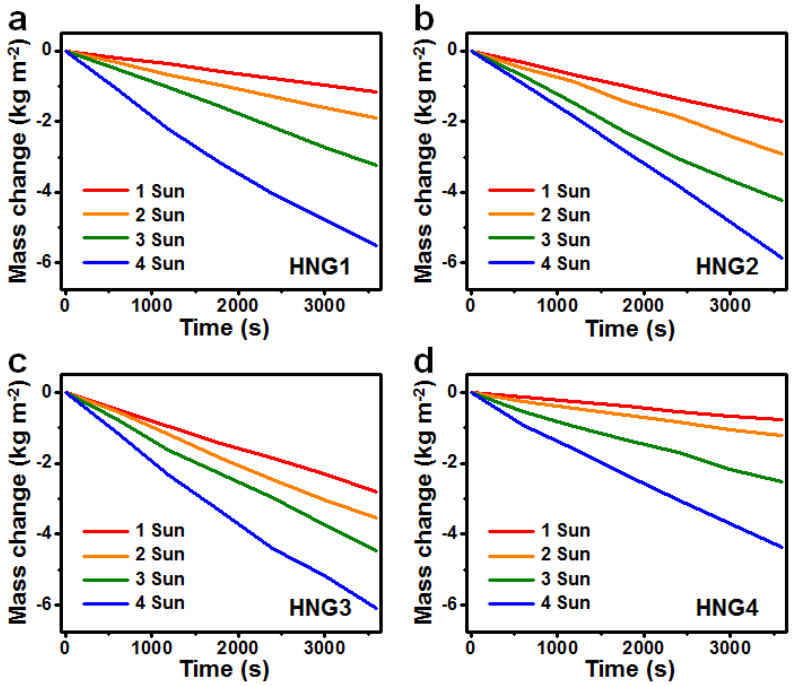

Supplementary Figure 15. Mass change over time with (a) HNG1, (b) HNG2, (c) HNG3 and (d) HNG4 under 1 to 4 sun (1 to 4 kW m^{-2}) radiation.

S2.13 Solar vapor generation based on pure PVA hydrogels.

The PVA gels with water/PVA weight ratio of 1:0.2, 1:0.15, 1:0.1 and 1:0.075 were prepared and noted as PVA1, PVA2, PVA3 and PVA4 to evaluate the solar vapor generation. The corresponding water evaporation rates were 0.32, 0.36, 0.35 and 0.35 kg/m^2/h, respectively.

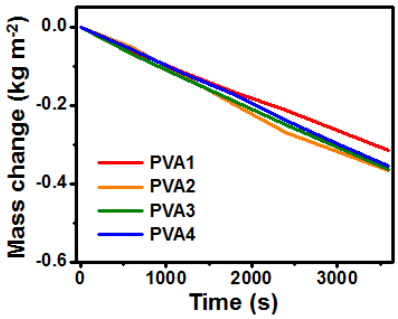

Supplementary Figure 16. Mass change over time with PVA gels.

S2.14 Equivalent evaporation enthalpy of water in HNGs.

To explain the evaporation latent heat reduction, we proposed a hypothesis that it is because water clusters existed in water tends to evaporate more easily when confined by the molecular meshes of HNGs during vaporization, which reduces the overall energy consumption (*Vide infra*). The water molecules in liquid phase have been demonstrated to be linked by hydrogen bonds, forming water clusters[S7] with minimized energy by their configuration variations[S8,S9]. As a result, every water molecule was confined to the dynamically stabilized clusters and bounded by adjacent clusters[S10]. Due to the hydrogen bonds between the hydrogel network and water molecules, some of those bounded clusters were activated. During the evaporation process, these water clusters might escape more easily from the PVA network into the air, contributing to the evaporation rate, and resulting in a lower energy requirement to evaporate certain amount of water. Therefore, the water evaporation enthalpy is reduced. To prove this hypothesis, we presented experimental data along with corresponding theoretical analysis in this section.

This section is organized as follows. In part S2.14.1, we extract a much smaller equivalent evaporation enthalpy of water in HNGs compared with pure water from evaporation rate measurement. The equivalent evaporation enthalpy is validated by differential scanning calorimetry (DSC) in part S2.14.2. To further understand the effect of hydrogel network on the evaporation enthalpy, the Raman spectroscopy was performed in part S2.14.3. It was identified that there were three modes of water molecules in the polymeric network distinctively different from bulk water, which can be categorized as free water (i.e. pure liquid water), intermediate water and bound water. In part S2.14.4, Using tracing Li^+ ion that is entrained with water clusters, we directly measured higher residual Li^+ concentration in the condensate water obtained from the evaporation of LiCl solution. Finally, we presented a thermodynamic analysis and formulate the enthalpy change of water evaporation upon the existence of water clusters in part S2.14.5.

S2.14.1 Estimation of Equivalent Evaporation Enthalpy

To obtain the vaporization enthalpy, we designed a control experiment to estimate the evaporation enthalpy. The water and HNG samples with same superficial area were synchronously set in a closed container together with the supersaturated potassium carbonate solution (enabling stabilized RH of ca. 45%) under a temperature of ca. 25 ºC and ambient air pressure. The water evaporation rate and corresponding calculated equivalent evaporation enthalpy (ΔH_{equ}) were shown in Supplementary Figure 17 a and b, respectively. The ΔH_{equ} of water in HNGs can be estimated vaporizing the water with identical power input (U_{in}), which has

$$U_{in} = \Delta H_{vap} m_0 = \Delta H_{equ} m_g$$

where ΔH_{vap} and m_0 were the evaporation enthalpy and mass change of bulk water; m_g was the mass change of HNG. The energy efficient was also calculated based on E_{equ} of corresponding HNG sample. The obtained equivalent evaporation enthalpy of water in HNG sample (e.g. ~1.3 kJ g^{-1} for HNG3) are greatly reduced compared with bulk water. Note that such equivalent enthalpy cannot be directly estimated in solar evaporation tests because the energy efficiencies are different under solar irradiation with various concentration.

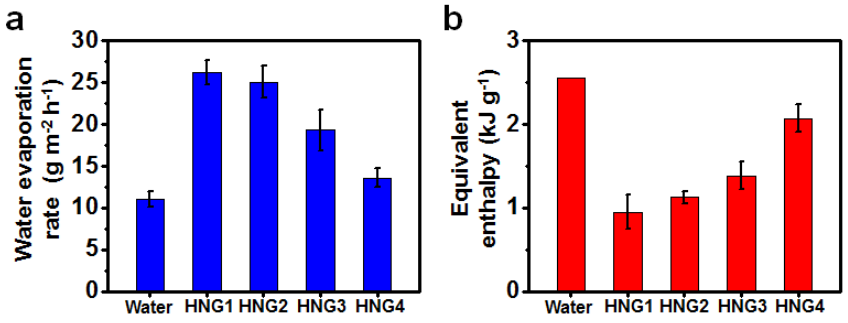

Supplementary Figure 17. (a) Water evaporation rate in dark condition and (b) the calculated equivalent enthalpy of with and without HNGs.

S2.14.2 DSC Measurement of Vaporization Enthalpy.

To prove the reduced evaporation enthalpy of water in HNGs, differential scanning calorimetric (DSC) measurement is used for measuring the vaporization energy of pure water and water in the hydrogel. Before measuring vaporization enthalpy of the hydrogel samples, sapphire is used as the reference material to calibrate the DSC and for further calculating the effective heat capacity of hydrogel samples. During the vaporization enthalpy measurements, the hydrogel was placed in an open Al crucible and measured with linear heating rate 5 K/min, under nitrogen flow flux (20 mL/min), in the temperature range from 30 to 200 °C[S11]. The effective specific heat capacity, C_{pe}, can be calculated by comparing the heat flow of measured hydrogels with that of the standard sapphire sample.

Supplementary Fig. 18 shows the change of heat flow signal as a function of temperature. For pure water, a sharp peak is observed and the heat flow signal decreased dramatically after the signal reaches maximum. This indicates the water evaporation is completed immediately. For all the four hydrogel samples we tested, the peaks are much broader than that of the pure water, and the heat flow signal showed a gradual decay instead, indicating that the water evaporation in hydrogel is different from pure water.

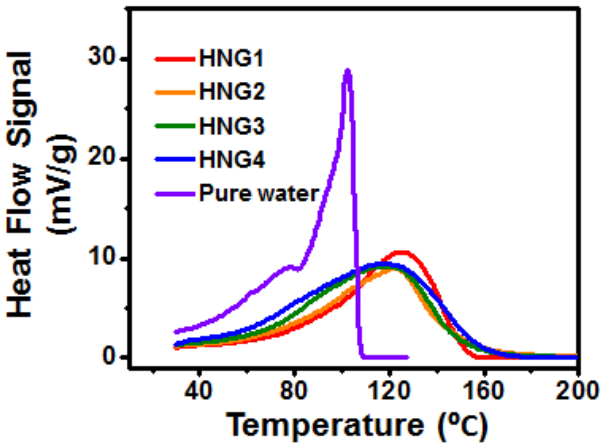

Supplementary Figure 18. Thermograms of hydrogels and pure water, the magnitudes of the DSC signal were proportional to the heat flow during the measurements.

Supplementary Table 1 summarizes the total mass, mass of water and the calculated vaporization enthalpy of pure water and the hydrogel samples. The measured enthalpy of water is 2417 J/g, which is very close to the theoretical value of 2444 J/g,[S12] indicating the accuracy of our measurements. The vaporization enthalpy of the water in the hydrogels is much smaller than that of pure water, due to influence of hydrogel network on the evaporation process. Note that the enthalpy values calculated for DSC are higher than those tested in evaporation experiment, since the DSC test and evaporation test present a full dehydration and slightly dehydration processes, respectively (See S2.14.3 for detailed difference).

Supplementary Table 1. Summary of DSC measurement results

	HNG 1	HNG 2	HNG 3	HNG 4	Pure water
Total mass (mg)	34.1	24.1	25.4	25.5	22.5
Water (mg)	30.7	20.3	20.8	22.8	22.5
Enthalpy (J/g)	1765	1702	1919	2148	2417

S2.14.3 Polymeric Network Enabled Activation of Water.

To prove the existence of different types of water molecules, we measured Raman Spectra of water confined in HNG, as shown in Supplementary Fig.19. The Raman spectra of (a) water (b) HNG3 and (c) HNG1 were fitted by four peaks through Gaussian function. The peaks observed at 3233, 3401, 3514, and 3630 cm^{-1} was related to water[S13]. These peaks are classified as two types of modes: (1) Water molecules with four hydrogen bonds, i.e., two protons and two electron pairs, are involved in hydrogen bonding (the peaks at 3233 and 3401 cm^{-1}); (2) weakly or non-hydrogen-bonded water molecules in which the hydrogen bonds of the water molecules have been broken, in part or entirely (the peaks at 3514 and 3630 cm^{-1}). Within the band corresponding to the four hydrogen-bonded molecules, the peak at 3233 cm^{-1} is associated with the collective in-phase vibrations of all molecules in the aggregate, whereas the 3401 cm^{-1}

peak is associated with vibration, which is not in-phase between the first and higher shell of neighboring molecules (i.e., the out-of-phase mode of O-H stretching).

The peaks at 3514 and 3630 cm^{-1} correspond to the symmetric and asymmetric stretching of the weakly hydrogen bonded H_2O molecules, respectively. The peak at 3050 cm^{-1} (light blue) is believed to arise from the Fermi resonance between the overtone of the bending mode. The peaks (gray) around 2800 cm^{-1} were raised by vibration of chemical bonds on PVA. The calculated molar ratio of intermediate water (IW): free water (FW) in pure water, HNG3 and HNG1 were 0.22:1, 0.71:1 and 0.79:1, respectively. We note that the relatively high ratio of intermediate water in pure water sample can be attributed to the surface tension induced hydrogen bonds weakening[S14]. These results indicate that most of water contained in HNGs are intermediate water, facilitating the water evaporation.

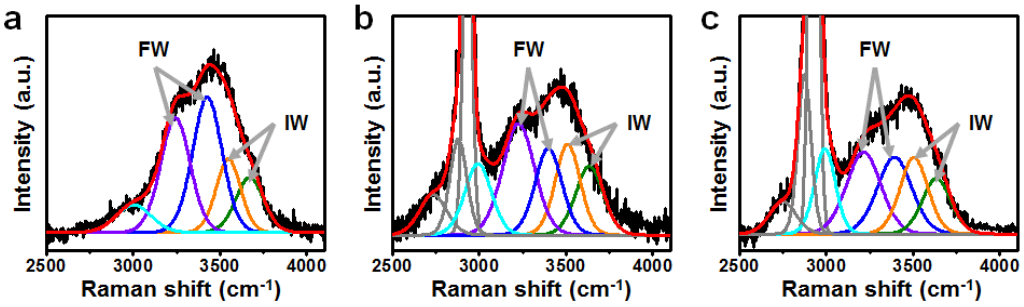

Supplementary Figure 19. Fitting curves in the energy region of O-H stretching modes for (a) water (b) HNG3 and (c) HNG1. The FW and IW represent free water and intermediate water, respectively.

S2.14.4. HNG Driven Evaporation of Water Clusters

Moreover, we believe that such latent heat reduction was due to evaporation of water clusters from molecular mesh confined water. Indeed, there has been a combined experiment of mass spectroscopy and velocity map imaging showing that, the mean velocity of vapor molecules increases with the decreasing size of water cluster[S15]. This suggest that it takes higher energy for a monomer to escape from bulk water compared

with water clusters. We therefore infer that the evaporation of water confined in the molecular mesh is more like water clusters, which reduces the effective vaporization enthalpy. To prove water-cluster evaporation, lithium chloride, a nonvolatile electrolyte which can be loaded by the water clusters[S16-S18], was added into the original bulk water. If this hypothesis is valid, the Li^+ can be carried to the condenser by the water clusters in the vapor, and finally accumulated in condensed water in a HNG-based evaporation system (Supplementary Fig. 20a). On the contrary, in the traditional evaporation system (Supplementary Fig. 20b), the concentration of Li^+ in the condensed water should be significantly lower.

Indeed, the Li^+ concentration tested by inductively coupled plasma mass spectrometry (ICP-MS) confirmed our hypothesis. As shown in Supplementary Fig. 20c, the concentration of Li^+ in condensed water from HNG-based evaporation presented a dependence on the concentration of LiCl in original water, while the condensed water from traditional evaporation showed a low concentration of Li^+ with no dependence on the Li^+ concentration of the original water. These results indicated that water evaporated from HNG-based system is more likely to be in clusters. Note that the concentration of Li^+ in the purified water is ~10^3 lower than that of original brine (~10^6 higher than that of natural seawater) after desalination. Key parameters for the evaluation of seawater desalination are the concentration of primary ions (Na^+, Mg^{2+}, K^+ and Ca^{2+}) after desalination as shown in Fig. 5 in the main text. These results indicate that the proposed system can work well for the solar desalination of seawater despite the potential minor residual of Li^+ or some other ions with strong solvation in water.

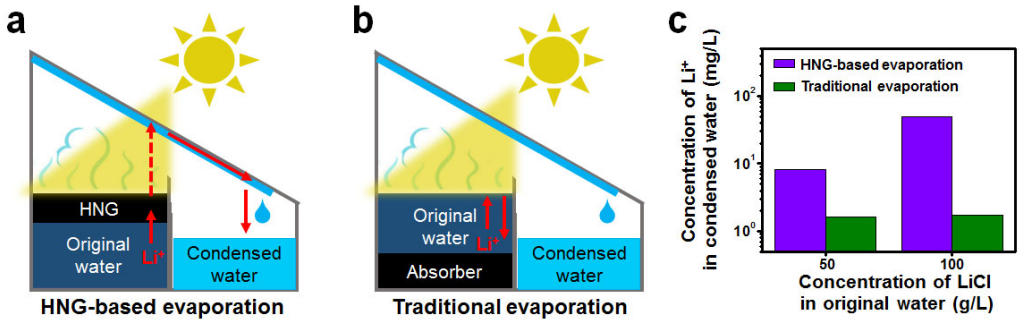

Supplementary Figure 20. The experimental setup of (a) HNG-based evaporation and (b) traditional evaporation. (c) The concentration of Li^+ in condensed water from different LiCl solutions HNG-based evaporation (violet) and traditional evaporation (green).

S2.14.5 Thermodynamic Analysis

The residual Li^+ concentration measurement in S2.14.4 clearly shows that certain amount of liquid water clusters might exist in the vapor phase. In this part, we qualitatively analyze the evaporation enthalpy reduction due to the existence of liquid water clusters.

First, we derive the formula for calculating ΔH_{vap} for pure water fully vaporized into gas molecules. By definition, the latent heat of water vaporization is the difference of enthalpy between the liquid phase and gas phase:

$$\Delta H_{vap} = H_{gas} - H_{l-water} \quad \text{(S1)}$$

where H_{gas} and $H_{l\text{-}water}$ are the enthalpy of the gas and liquid phase, respectively. Since

$$H = E + pV \quad \text{(S2)}$$

where H is the internal energy, p is the pressure and v is the volume, the enthalpy of the gas phase is written as:

$$H_{gas} = E_{gas} + pV_{gas} \quad \text{(S3)}$$

The internal energy of the gas E_{gas} is a summation of potential energy U_{gas} and kinetic energy K_{gas}:

$$E_{gas} = K_{gas} + U_{gas} = K_{gas} + U_{gas}^{intra} + U_{gas}^{inter} \quad \text{(S4)}$$

where U_{gas} can be further classified into intermolecular potential U_{gas}^{inter} (*i.e.* the potential energy between different water molecules) and the intramolecular potential U_{gas}^{intra} (*i.e.* the potential energy of the bonding within each water molecules). Substituting Eq. (S4) into Eq. (S3), we obtain:

$$H_{gas} = K_{gas} + U_{gas}^{intra} + U_{gas}^{inter} + pV_{gas} \quad \text{(S5)}$$

For water vapor at room temperature at 1atm, the intermolecular potential is negligible and we can regard water vapor as ideal gas, thus $pV_{gas} = Nk_BT$ where N is the number of water molecules, k_B is the Boltzmann constant and T is the temperature[S19]. The Eq. (S5) can therefore be written as:

$$H_{gas} = K_{gas} + U_{gas}^{intra} + Nk_BT \quad \text{(S6)}$$

For the liquid water phase:

$$H_{l-water} = E_{l-water} + pV_{l-water} \quad \text{(S7)}$$

The internal energy of the liquid phase can also be written as a summation of kinetic energy K_{liquid}, intermolecular potential $U_{l-water}^{inter}$ and $U_{l-water}^{intra}$, $E_{l-water} = K_{l-water} + U_{l-water}^{inter} + U_{l-water}^{intra}$, and the enthalpy of liquid water is:

$$H_{l-water} = K_{l-water} + U_{l-water}^{inter} + U_{l-water}^{intra} + pV_{l-water} \quad \text{(S8)}$$

The vaporization enthalpy is therefore:

$$\Delta H_{vap} = \left(K_{gas} - K_{l-water}\right) - U_{l-water}^{inter} + \left(U_{gas}^{intra} - U_{l-water}^{intra}\right) + (Nk_BT - pV_{l-water}) \quad \text{(S9)}$$

At the same temperature, the kinetic energy of water molecules in liquid phase and gas phase is identical, therefore, $K_{gas} - K_{l-water} = 0$. The vibrational energy of bonds in each water molecule should also stay the same no matter in the gas or the liquid phase, so $U_{gas}^{intra} - U_{l-water}^{intra} = 0$. For the same amount of molecules, the volume of liquid water should be much smaller than the volume of water vapor, therefore $Nk_BT = pV_{gas} \gg pV_{l-water}$. Eq. (S9) can therefore be simplified to:

$$\Delta H_{vap} = -U_{l-water}^{inter} + Nk_BT \quad \text{(S10)}$$

The $U_{l-water}^{inter}$ in Eq. (S10) is indeed the cohesive energy of the liquid water. Eq. (S10) also indicates that the vaporization latent heat of fully vaporized water is mainly directly by the intermolecular potential energy.[S16] To validate our theoretical derivation, we performed an MD simulation, and we obtained a vaporization enthalpy of 2438 kJ/kg (see details in part S2.14.3), agreeing well with previously reported MD calculations [S19,S20].

Now we consider the vaporization enthalpy of water when liquid water clusters exist in the steam phase. The enthalpy of the vapor with liquid cluster is written as a weighted average:

$$H_{vap-cluster} = \chi H_{gas} + (1 - \chi)H_{cluster} \quad \text{(S11)}$$

where H_{gas} is the enthalpy of pure vapor gas, and $H_{cluster}$ is the enthalpy of the liquid water clusters in the vapor, and χ, termed vapor quality, is the fraction of gas molecules in the steam phase. The vaporization enthalpy is therefore:

$$\Delta H_{vap-cluster} = H_{vap-cluster} - H_{l-water} \quad \text{(S12)}$$

Substitute Eq. (S11) into Eq. (S12), the vaporization enthalpy of water confined in NHGs is composed of two parts:

$$\Delta H_{vap-cluster} = \chi \Delta H_{vap} + (1 - \chi)\Delta H_{cluster} \quad \text{(S13)}$$

where ΔH_{vap} already defined in Eq. (S1) is the enthalpy change for water in hydrogel to be fully vaporized to gas phase, and $\Delta H_{cluster}$ is the enthalpy change for a cluster to escapte the gel network. Similar to the derivation of Eq. (S10), the enthalpy for clusters to escape from the surrounding water molecules is:

$$\Delta H_{cluster} = -U_{cluster-water} + Nk_BT \quad \text{(S13)}$$

where $-U_{cluster-water}$ is the energy it takes for clusters to escape from the water. Substituting (S12) and (S13) into (S11), the evaporation enthalpy of the gel is obtained as:

$$\Delta H_{vap-cluster} = -\left[\chi U_{l-water}^{inter} + (1-\chi)U_{cluster-water}^{inter}\right] + Nk_BT \quad \text{(S14)}$$

Subtracting (S14) from (S10), we obtain the change of evaporation enthalpy:

$$\Delta H_{vap-cluster} - \Delta H_{vap} = (1-\chi)[(-U_{cluster-water}^{inter}) - (-U_{l-water}^{inter})] \quad \text{(S15)}$$

Equation (S15) shows that the vaporization enthalpy is changed due to the existing liquid water clusters in the steam. Although it is difficult to obtain the exact value of $(-U_{cluster-water}^{inter})$, we can still say that $[(-U_{cluster-water}^{inter}) - (-U_{l-water}^{inter})]$ <0. This is because the energy per molecule required for a cluster to escape from the surrounding liquid is smaller compared with a single molecule. For a single molecule to evaporate, all the hydrogen bonds with its neighboring molecules are broken, but for the water cluster, only the hydrogen bonds at cluster surface are broken the hydrogen bonds within the water cluster remained intact. Therefore, $\Delta H_{vap-cluster} < \Delta H_{vap}$

We illustrate the evaporation latent heat with and without the HNGs in Supplementary Figure 21. The vaporization enthalpy is considerably reduced for the vapor produced with HNGs, due to the existence of liquid water clusters in the steam phase (i.e. lower vapor quality χ). This analysis agrees with the residual Li^+ measurement.

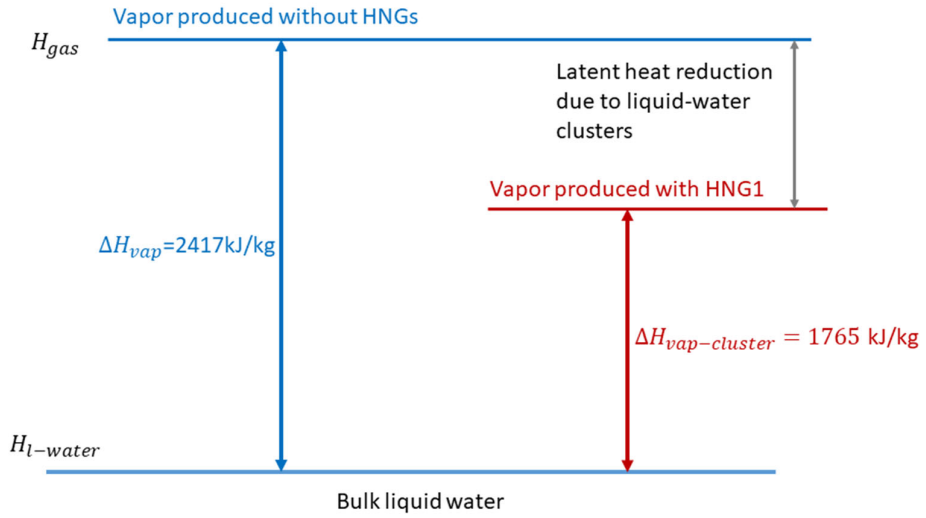

Supplementary Figure 21. Schematic illustrating the reduced vaporization enthalpy due to the evaporation of water clusters assisted by HNG molecular mesh. Horizontal lines and vertical arrows show the enthalpy level of each state and enthalpy change in the solar desalination process, respectively.

MD simulation details. We performed a molecular dynamics (MD) simulation showing that the vaporization enthalpy (ΔH_{vap}) of water is solely determined by the inter-molecular potential energy of water molecules. All MD simulations are performed using the LAMMPS package[S21].

Based on the analysis above, we first calculated the vaporization enthalpy of pure water. TIP3P potential[S22] is used in MD simulation. Remarkably, if we simply distribute water molecules randomly in the simulation box with initial density equal to bulk water, there is great chance that the distance between some water molecules are too close to each other, resulting in an explosive increase of the volume of the simulation cell. To solve this problem, we randomly distribute 2000 water molecules within a box with side length of 70 Å as the initial structure (initial density $\rho = 0.174$ kg/m^3), with the help of Packmol package[S23,S24]. Such a low initial density ensures that the distance between water molecules is long enough, so that the nonphysical increase of the volume due to the strong repulsive force between molecules can be avoided. We then slowly heated up the water molecules by thermalizing the structure at 1 K, 10 K, 50 K, 100 K, 200 K and 300 K using isobaric-isothermal (NPT) ensemble. For each temperature listed, we equilibrating the system for 100 ps, with a time step of 0.1 fs. Supplementary Fig. 22a shows the obtained simulation cell of the liquid water at 300 K containing 2000

H_2O molecules. The final density $\rho = 0.996$ kg/m^3. After obtaining the atomic structure of liquid water, we further performed the MD simulation under NPT ensemble for 500 ps, and the total intermolecular potential $U_{l-water}^{inter}$ is sampled every 50 fs. The calculated specific latent heat of pure water is $h_{vap} = 2438$ kJ/kg (Supplementary Fig. 22b), agreeing well with previously reported MD calculations[S19,S20].

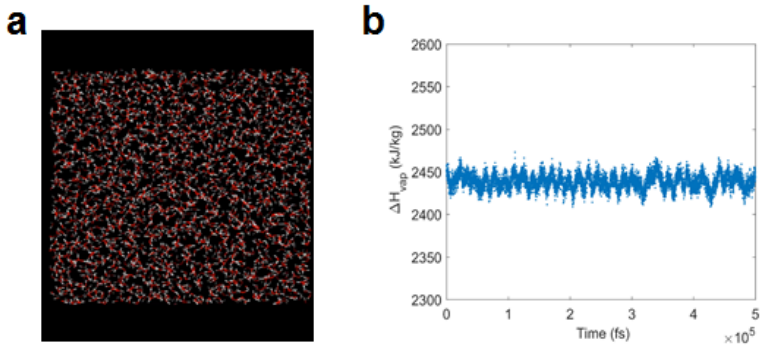

Supplementary Figure 22. (a) A cubic simulation cell of liquid water containing 2200 water molecules at 1atm and 300 K. Periodic boundary condition is imposed on each direction. (b) The calculated specific vaporization enthalpy.

To sum, the physical mechanism of reduced enthalpy proposed here is well in agreement with the prior literature, which shows polymer mesh induced enthalpy reduction. The key structure to reduce the enthalpy in current work is the polymeric network, rather than micro-channels (consisted by micropores) that only act as water pathways through the HNG. The hierarchical structure presented in current work (as shown in Fig. 1) is the better structure because such structure not only enables the reduced enthalpy based on polymeric network but also overcomes the drawback of slow water transport in other uniform polymeric networks.

S2.15 Energy efficiency of HNG3 under concentrated solar irradiation.

When the water evaporation is accelerated by the concentrated solar irradiation, the water transport designed for 1 sun (for HNG-3) becomes inadequate and, thus, the heat localization behavior of HNG will be changed. As shown in Supplementary Fig. 23a, the surface temperature of HNG3 increased with the concentration of solar irradiation, indicating an efficient solar absorption. In addition, the temperature of bulk water increased with the concentration of solar irradiation, suggesting an energy loss to the bulk water. We have calculated the corresponding energy efficiency under various sun flux (Supplementary Fig. 23b) and the results show that the energy efficiencies decreased with the increase of sun flux.

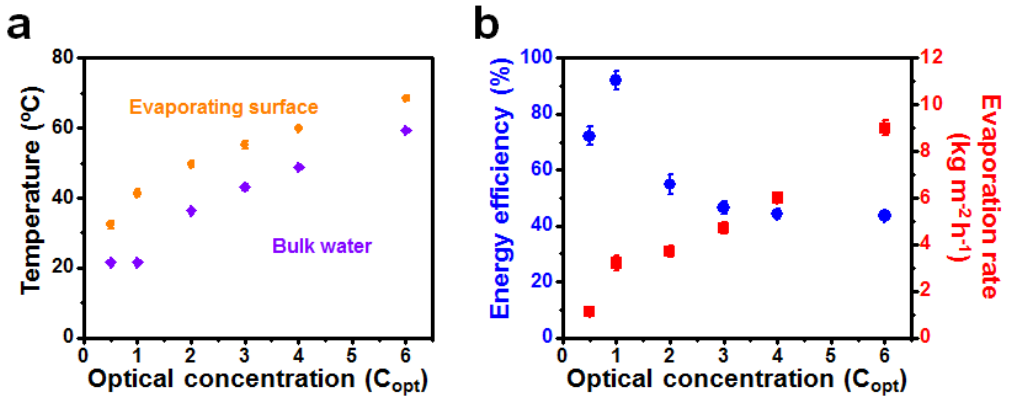

Supplementary Figure 23. (a) Temperature of evaporating surface of HNG3 and bulk water underneath the HNG3 upon exposure to concentrated solar irradiation. (b) Energy efficiency with corresponding evaporation rate of HNG3 under concentrated solar irradiation.

S2.16 Recent achievements on improving solar energy efficiency.

Along with previous reports, the energy efficiency could be improved by concentrating the solar radiation[S25-S29]. For instance, despite an energy efficiency of 65 % under one sun, a graphene-based material can utilize 85 % of converted solar energy under 10 times concentrated solar radiation[S25]. Owing to the advanced nanostructure and/or special properties of novel materials, the highly efficient energy utilization was gradually achieved with weaker solar flux[S26,S27]. As shown in Supplementary Figure 24, an energy efficiency of 90 % was realized under 4 kW m^{-2} solar radiation[S28], while the record upon solar flux of 10 kW m^{-2} has been raised to 94.8 %[S29]. Herein, our HNG, for the first time, enabled an energy efficiency up to 93.5 % under 1 kW m^{-2} solar radiation, opening the possibility for harvesting natural sunlight as a source of energy.

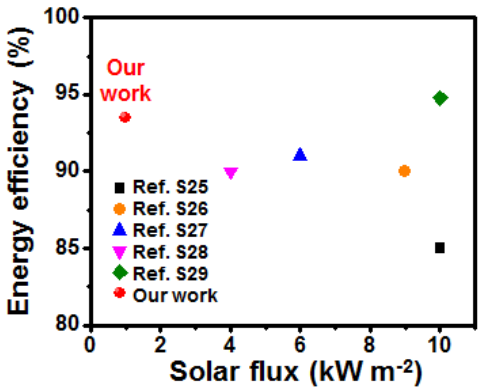

Supplementary Figure 24. Achievements of solar energy efficiency based on novel solar vapor generators in recent years.

S2.17 COMSOL Simulation of temperature distribution in HNGs.

Considering the water confinement of polymeric network and the convection in the internal gaps and micron channels, the heat transfer in HNGs could be described by the equation given below:

$$E_{in} = \rho C_p \frac{\partial T(x,t)}{\partial t} + \rho C_p v \cdot \nabla T(x,t) + \nabla [k \nabla T(x,t)]$$

Where the x and t are the space vector and time, respectively; ρ, C_p, and T (x, t) are the mass density, liquid thermal capacity and the local temperature, respectively; ν and k is the fluid flow speed and thermal conductivity of the aqueous medium; E_{in} represents the thermal energy input from the optical-thermal conversion. Along with the previous report, the heat transfer model can be simplified as a semi-infinite medium for the Cartesian coordinate system [S23]. The numerical simulations are conducted by COMSOL Multiphysics 4.4, under the steady and transient analysis mode. Wherein, a constant heat flux of 0.1 kW m^{-2} occurs on the top (Z = 500), corresponding to the solar energy input on the surface of HNG (the evaporation consumed the energy of ca 0.9 kW m^{-2}). The 2D model is discretized into 1,000 elements. The convection heat transfer in the polymeric network was disabled to describe the water restriction effect. To carry out a qualitative analysis, we assume that the temperature of environment and water was set to 20 ºC (293 K); the balanced heat flux was 0.1 kW m^{-2}. In the transient mode simulation, the initial and final condition of transient analysis was set to t = 1 s and t = 6000 s, respectively. As consequence, the temperature distribution in HNG slightly varies with time due to the continuous photothermal conversion (heating) and evaporation process (cooling) occurred around the surface (Supplementary Figure 25).

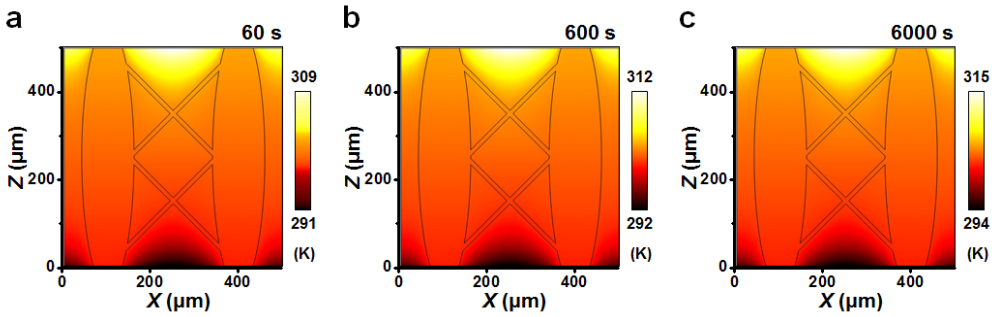

Supplementary Figure 25. Transient state simulation of temperatures distribution at (a) 60 s, (b) 600 s and (c) 6000 s.

S2.18 COMSOL Simulation of water transport in HNGs.

As mentioned in the main text, we derive a steady model for water transport in HNG based on the biphasic mixture theory, which combines the flow of a fluid through a porous medium with different porosities and ignores the complexity caused by deformation. The network of the polymer and the penetrating fluid in the hydrogel will be taken as the penetrable solid and fluid, respectively[S30]. In the hydrogel, we consider conservation of mass for the water phase of the fully swollen hydrogel as:

$$\nabla \cdot \nu_p = \nabla \cdot \left[\phi_w \cdot \left(\nu_p - \nu_w\right)\right]$$

where ϕ_w is the water volume fraction, ν_p and ν_w are the intrinsic velocity of polymer and water phases, respectively. Meanwhile, the conservation of momentum for the polymer and fluid phase are given, respectively, by:

$$\nabla \cdot \sigma_p + f_{pw}\left(\nu_w - \nu_p\right) = 0$$

$$\phi_w \nabla \cdot P + \sum f_{iw}(\nu_w - \nu_i) = 0$$

Where σ_p, and f are the stress tensor and drag force between the two phases; P represents the intrinsic fluid pressure, comprising the osmotic pressure and the remaining part of the intrinsic fluid pressure. Along with the experimental data, the predetermined ν_{w0} was set on the top boundary of the polymeric skeleton. Numerical simulations are conducted by COMSOL Multiphysics 4.4, under the steady analysis mode. The 2D model is discretized into 1,000 elements. To carry out a qualitative analysis, we also assume that the $f_{wp} = 10^{12}$ N s m^{-2} in the polymeric network to simplify the calculation[S30]. As shown in Supplementary Figure 26, the calculated ν_w was varied with the change of predetermined ν_{w0}, indicating a responsive water transport responsive toward the water evaporation.

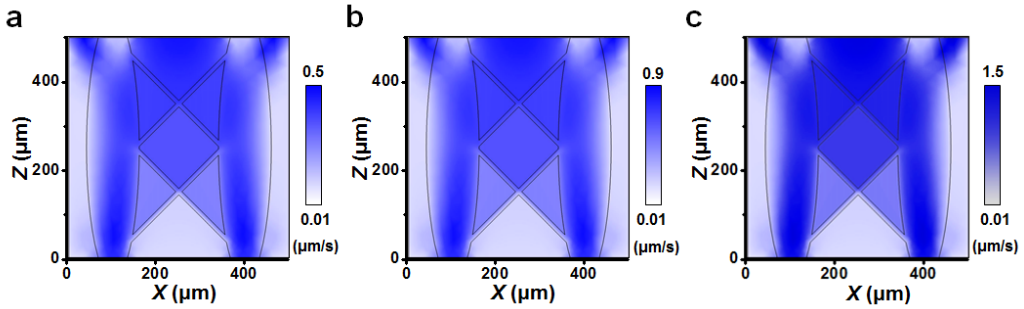

Supplementary Figure 26. Steady state simulation of water transport upon surficial water loss of (a) 0.45, (b) 0.89 and (c) 1.45 μm s^{-1}.

S2.19 Conductance salinity measurement.

The salinity and conductance of NaCl solution exhibited linear dependency in a range of salinity from 0.001 to 0.01 ‰. The standard curve was established for the calculation of salinity of purified water from artificial seawater (Supplementary Figure 27a). To accurately calculate the salinity, the conductance was tested from three parallel samples and the calculation was carried out through an average value (Supplementary Figure 27b).

a

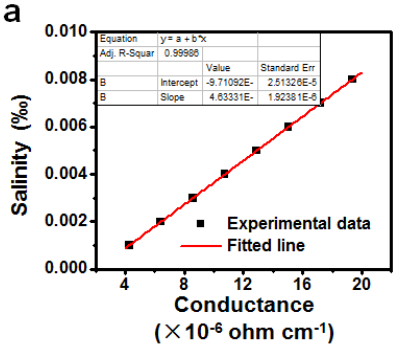

b

Original salinity of original samples (‰)	8	35	100
Conductance test 1 (×10^{-6} ohm cm^{-1})	9.83	6.07	14.24
Conductance test 2 (×10^{-6} ohm cm^{-1})	9.80	6.28	13.72
Conductance test 3 (×10^{-6} ohm cm^{-1})	9.91	6.24	14.22
Average conductance (×10^{-6} ohm cm^{-1})	9.85	6.20	14.06
Calculated salinity of purified samples (‰)	0.003592	0.001894	0.005552

Supplementary Figure 27. (a) Linear dependency of salinity and conductance of NaCl solution under 25 ^{o}C. (b) The calculated salinity of purified water through conductance tests.

S2.20 Comparison of solar vapor generation in open and closed systems.

To clarify the influences of humidity and solar radiation intensity, the laboratory experiment of "one sun solar evaporation in closed system" (denoted as closed-1- sun) and "open system evaporation under weak solar radiation (open-0.5 sun)" were carried out (Supplementary Fig. 29). As shown below, the tested evaporation rate in closed-1-sun experiment was ca. 2.7 kg/m^2/h, which is lower than ca. 3.2 kg/m^2/h in standard experiment (one sun, open system) with the same piece of HNG3 sample. This result indicated that the saturated humidity slightly reduced the evaporation of water. Additionally, the tested evaporation rate (ca. 1.2 kg/m^2/h) from open-0.5-sun experiment was lower than half of corresponding value under one sun (ca. 1.6 kg/m^2/h), suggesting that the decrease of solar energy input can dramatically reduce the evaporation rate, which is in good agreement with the classic solar still development literature. Therefore, the solar flux was the key factor to drive the decreased evaporation rate in our outdoor experiments. Note that all the tests based on open systems were proceeded at RH of ca. 45 % (ambient RH in our lab), and the presented values have been subtracted by the corresponding dark data.

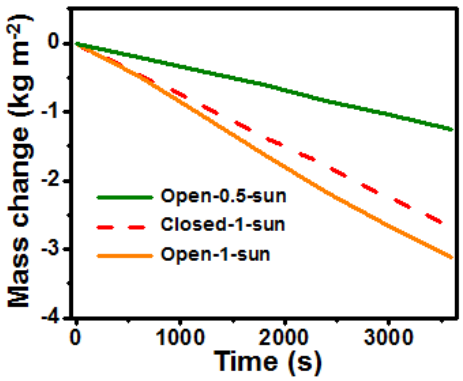

Supplementary Figure 28. Mass change over time with HNG3 upon different experimental conditions.

S2.21 Outdoor vapor generation under natural sunlight.

Supplementary Fig. 30 shows a measurement on days with different weather condition. In view of the solar flux variation caused by cloud cover, the average value of the irradiation over 12 hours (sunshine duration) was used to evaluate the energy input. As shown in Supplementary Fig. 30, day 1, 2, 3, 4, 7, are sunny days, day 8, 9, 10 are cloudy days, and day 5, 6 are rainy (overcast) days. The yield of purified water based on HNG water purification system (as mentioned in main text) was demonstrated to be higher than 600 mL per day in sunny days and almost 300 mL per day in cloudy days, vividly revealing the ability of the HNG to rapidly purify water during periods of low and varying solar flux, such as during non-summer months and cloudy days. Owing to the sunshine duration in different seasons (from 9 h to 14 h), the daily yield of purified water from HNG can be estimated to be 18 to 23 L m^{-2} in sunny days.

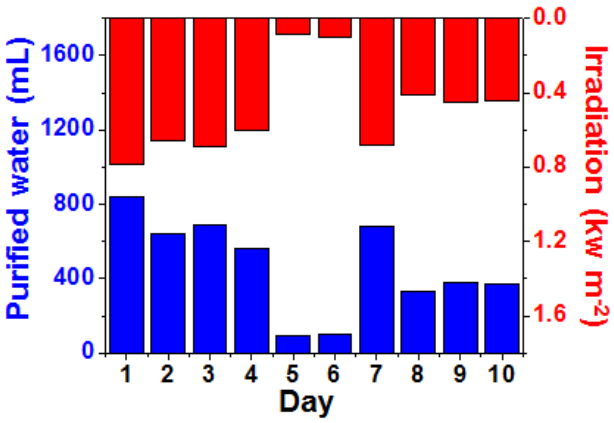

Supplementary Figure 29. The yield of purified water (Blue) from prototype water purification system for 10 days with corresponding average solar irradiation data (Red).

S3. Supplementary References

S1. Shi, Y. *et al*. A conductive self-healing hybrid gel enabled by metal–ligand supramolecule and nanostructured conductive polymer. *Nano Lett.* **15**, 6276-6281 (2015).

S2. Wang, Y. *et al.* Dopant-enabled supramolecular approach for controlled synthesis of nanostructured conductive polymer hydrogels. *Nano Lett.* **15**, 7736-7741 (2015).

S3. Bae, K. *et al.* Flexible thin-film black gold membranes with ultrabroadband plasmonic nanofocusing for efficient solar vapour generation. *Nature Commun.* **6**, 10103 (2015).

S4. Zielinski, M. S. *et al.* Hollow mesoporous plasmonic nanoshells for enhanced solar vapor generation. *Nano Lett.* **16**, 2159-2167 (2016).

S5. Zhang, L., Tang, B., Wu, J., Li, R., & Wang, P. Hydrophobic light‐to‐heat conversion membranes with self‐healing ability for interfacial solar heating. *Adv. Mater.* **27**, 4889-4894 (2015).

S6. Neumann, O. *et al.* Solar vapor generation enabled by nanoparticles. *ACS Nano* **7**, 42-49 (2012).

S7. Okumura, M., Yeh, L. I., Myers, J. D. & Lee, Yuan T. Infrared spectra of the solvated hydronium ion: Vibrational predissociation spectroscopy of mass-selected H_3O^+.cntdot.(H_2O)n.cntdot.(H_2)m. *J. Phys. Chem.* **94**, 3416-3427 (1990).

S8. Jiang, J-C. Infrared spectra of $H^+(H_2O)_{5-8}$ clusters: Evidence for symmetric proton hydration. *J. Am. Chem. Soc*. **122**, 1398-1410 (2000).

S9. Miyazaki, M., Fujii, A., Ebata, T. & Mikami, N. Infrared spectroscopic evidence for protonated water clusters forming nanoscale cages. *Science* **304**, 1134-1137 (2004).

S10. Sekine, Y. & Ikeda-Fukazawa, T. Structural changes of water in a hydrogel during dehydration. *J. Chem. Phys.* **130**, 034501 (2009).

S11. Von Solms, N., Koo, K. Y. & Chiew, Y. C. Mixing rules for binary Lennard-Jones chains: theory and Monte Carlo simulation. *Fluid Phase Equilib*. **180**, 71-85 (2001).

S12. Bellich, B., Borgogna, M., Cok, M. & Cesàro, A. Water evaporation from gel beads. *J. Therm. Anal. Calorim*. **103**, 81–88 (2011).

S13. Monosmith, W. B. & Walrafen, G. E. Temperature dependence of the Ramen OH-stretching overtone from liquid water. *J. Chem. Phys*. **81**, 669 (1986).

S14. Kudo, K., Ishida, J., Syuu, G., Sekine, Y., & Ikeda-Fukazawa, T. Structural changes of water in poly (vinyl alcohol) hydrogel during dehydration. *J. Chem. Phys.* **140**, 044909 (2014).

S15. Abdoul, C. *et al.* Velocity of a molecule evaporated from a water nanodroplet: maxwell–boltzmann statistics versus non‐ergodic events." *Angew. Chem. Int. Ed.* **54**, 14685-14689 (2015).

S16. Rodgers, M. T., & Peter B. Armentrout. Collision-Induced Dissociation Measurements on Li^+ (H_2O) n, n= 1-6: The First Direct Measurement of the $LiOH_2$ Bond Energy. *J. Phys. Chem. A,* **101.7**, 1238-1249 (1997).

S17. Bacelo, Daniel E., & Yasuyuki Ishikawa. Theoretical study of microscopic solvation of LiCl in water clusters: LiCl (H_2O) n (n= 1–4). *Chem. Phys. Lett.* **319.5**, 679-686(2000).

S18. Li, X., & Yang Z. Z. Study of lithium cation in water clusters: Based on atom-bond electronegativity equalization method fused into molecular mechanics. *J. Phys. Chem. A,* **109.18**, 4102-4111 (2005).

S19. Wang, J. & Hou, T. Application of molecular dynamics simulations in molecular property prediction. 1. density and heat of vaporization. *J. Chem. Theory. Comput*. **7**, 2151-2165 (2011).

S20. Ilčin, M. *et al.* Water liquid-vapor equilibrium by molecular dynamics: Alternative equilibrium pressure estimation. *Acta Chimica. Slovaca*. **9**, 36-43 (2016).

S21. Plimpton, S. Fast parallel algorithms for short-range molecular dynamics. *J. Comput. Phys*. **117**, 1-19 (1995).

S22. Jorgensen, W. L., Chamdrasekhar, J. & Madura, J. D. Comparison of simple potential functions for simulating liquid water. *J. Chem. Phys*. **79**, 926-935 (1983).

S23. Martínez, L., Andrade, R., Birgin, E. G. & Martínez, J. M. PACKMOL: A package for building initial configurations for molecular dynamics simulations. *J. Comput. Chem*. **30**, 2157-2164 (2009).

S24. Dauber-Osguthorpe, P. *et al.* Structure and energetics of ligand binding to proteins: Escherichia coli dihydrofolate reductase-trimethoprim, a drug-receptor system. *Proteins* **4**, 31-47 (1988).

S25. Hadi, G. *et al.* Solar steam generation by heat localization. *Nat. Commun.* **5**, 5449 (2014).

S26. Liu, Y. *et al.* A bioinspired, reusable, pape-based system for high−performance large−scale evaporation. *Adv. Mater.* **27**, 2768–2774 (2015).

S27. Zhou, L. *et al.* 3D self-assembly of aluminium nanoparticles for plasmon-enhanced solar desalination. *Nature Photon.* **10**, 393–398 (2016).

S28. Zhou, L. *et al.* Self-assembly of highly efficient, broadband plasmonic absorbers for solar steam generation. *Sci. Adv.* **2**, e1501227 (2016).

S29. Liu, Z. *et al.* Extremely cost−effective and efficient solar vapor generation under nonconcentrated illumination using thermally isolated black paper. *Global Challenges* **1**, 1600003 (2017).

S30. Chen, X. *et al.* Performance inhomogeneity of gelatin during gelation process. *Polymer* **50**, 6186-6191 (2009).